JOURNAL OF MATERIALS SCIENCE **34** (1999) 1419–1437

Combined atomistic–crystal plasticity analysis of the effect of beta phase precipitates on deformation and fracture of lamellar $\gamma + \alpha_2$ titanium aluminide

M. GRUJICIC, Y. ZHANG
Program in Materials Science and Engineering, Department of Mechanical Engineering, Clemson University, Clemson, SC 29634, USA

Atomistic simulations based on the use of interatomic potentials and a finite element method based on the crystal plasticity theory are combined to investigate the deformation and fracture behaviour of polycrystalline lamellar γ-TiAl + α_2-Ti_3Al material containing 10 vol % of body centred cubic beta phase precipitates. The effects of both stable beta phase precipitates, which deform by slip, and metastable beta phase precipitates, which deform by a combination of stress-induced martensitic transformation and slip, are studied. To model the cracking along the grain boundaries and the matrix–precipitate interfaces, the grain boundaries and interfaces are modelled using a cohesive zone approach. The grain boundary–interface potentials are determined by carrying out atomistic simulations of the grain boundary–interface normal separation (decohesion) and sliding.

The results obtained suggest that incompatibilities in the plastic flow between the adjacent grains in the single-phase material give rise to a large build-up in tensile hydrostatic stress in the region surrounding certain three-grain junctions, which, in turn, leads to nucleation of the grain boundary cracks and ultimate failure. The stable beta phase precipitates located at the three-grain junctions in the two-phase material help accommodate the incompatibilities in plastic flow, doubling the strain to failure. The lattice expansion, which accompanies martensitic transformation in the metastable beta phase precipitates, further delays nucleation of the grain boundary–interface cracks giving rise to an additional increase in the fracture strain.

1. Introduction

Two-phase γ-TiAl + α_2-Ti_3Al alloys with fine scale (approximately 1–2 μm) lamellar microstructure have received considerable attention over the last ten years, due to their enhanced ductility and fracture toughness (e.g. [1]). The enhanced ductility and fracture toughness are attained primarily in the single-crystalline form of these alloys. Contrary, polycrystalline forms of these materials are generally brittle and fail in tension at strains less than 3%. While single-crystal properties are quite attractive, a wide-scale application of the single crystalline form of these alloys is cost prohibitive. Consequently, over the last decade, there has been a great deal of research effort aimed at identifying and incorporating various means of the improvement of tensile ductility and fracture toughness in conventionally processed polycrystalline γ-TiAl + α_2-Ti_3Al based materials. One of the very promising approaches for the enhancement of ductility and toughness is the introduction of ductile grain-boundary precipitates, which assist the accommodation of the plastic flow incompatibilities across the grain boundaries caused by an insufficient number of slip systems in the matrix phase. Recently, Grujicic and Dang reported a significant enhancement (approximately 80%) in the ductility and fracture toughness of lamellar $\gamma + \alpha_2$ containing 10 vol % of Ti–V–Al based body centred cubic (b.c.c.) beta phase precipitates [2].

Over the last two decades, various investigations have clearly established that stress-induced martensitic transformations can significantly enhance tensile ductility and fracture toughness of ZrO_2 and various ceramics containing ZrO_2 as the second phase (e.g. [3]), as well as of ultra-high strength secondary-hardened steels (e.g. [4]). The fundamental basis for comprehending the phenomenon of martensitic transformation–enhanced ductility and toughness resides in the thermodynamics and associated kinetics of the stress-assisted transformation. A materials constitutive model, which is based on the thermodynamics and the kinetics of deformation-induced martensitic transformation, has been recently proposed by Grujicic and Sankaran [5, 6]. The model describes transformation plasticity accompanying stress-assisted martensitic transformation in metastable particles embedded into a stable non-transforming matrix. Grujicic and Sankaran subsequently used a

continuum composite approximation to analyse the material system consisting of metastable Ti–Al–V–Fe based b.c.c. beta phase particles embedded into the lamellar $\gamma + \alpha_2$ titanium aluminide matrix. Within the continuum composite approximation, each material point is considered to consist of fixed volume fractions of γ, α_2 and β. This approach allowed determination of the effect of transformation-controlled plasticity in the beta phase on the stress and displacement fields in the crack-tip region as well as in the necking region where the strain is being localized. The continuum composite approximation, however, does not allow a study of the role of incompatibility in the plastic flow across the matrix grain boundaries on intergranular cracking and fracture. In a recent study Grujicic and Zhang [7] carried out a crystal plasticity finite element analysis of deformation and fracture of a γ-TiAl + α_2-Ti_3Al material containing 10 vol % of either stable (non-transforming) or metastable (transforming) beta phase precipitates located at the three-grain junctions. This analysis revealed the beneficial effects of the ductile beta phase in accommodating the incompatibility in plastic deformation between the adjacent matrix grain. It also showed that, due to lattice expansion associated with the transformation, metastable beta phase precipitates delay the onset on grain boundary decohesion thus further enhancing tensile ductility.

In the present work, the crystal plasticity analysis carried out by Grujicic and Zhang [7] is extended to elucidate further the mechanism by which both stable and metastable beta phase grain boundary precipitates enhance ductility and fracture toughness of the lamellar $\gamma + \alpha_2$ titanium aluminide. The analysis is carried out using the commercial finite element code ABAQUS [8]. The cohesion-zone type potentials [9] for the matrix grain boundaries and the matrix–precipitate interfaces are determined using the atomistic simulation (molecular statics) analysis and subsequently used to derive the corresponding (continuum-type) grain boundary–interface elements stiffness matrix.

Notation used in the present paper is based on the following conventions: scalars are written in regular type (e.g. f, γ, σ), vectors using boldface lowercase Roman, (e.g. **e**, **t**), second-order tensors as boldface uppercase (e.g. **T**, **D**), while fourth-order tensors use capital boldface italics (e.g. ***I***, ***J***). Tensor (dyadic) products are indicated by $\otimes$, tensor scalar products of appropriate order by x. The norm and the transpose of a second-order tensor **A** are denoted by $\|\mathbf{A}\|$ and $\mathbf{A}^{\mathbf{T}}$, respectively.

The organization of the paper is as follows. The materials constitutive relations for the matrix phase and the precipitate (dispersed) phase are discussed in Section 2.1. The atomic-scale procedure used for calculation of the grain boundary and interface potentials is presented in Section 2.2. The details of the finite element method used and its implementation as well as the procedure for determination of the stiffness matrix of the grain boundary–interface finite elements are presented in Section 2.3. In Section 3, the main results of the present work are presented and discussed. The main conclusions drawn from the present study are given in Section 4.

2. Experimental

2.1. Materials constitutive relations

The deformation behaviour of the three crystalline phases (gamma, alpha-2 and beta) encountered in the present case is represented using the formulation of the elastic–viscoplastic crystalline slip constitutive theory developed by Pierce *et al.* [10, 11]. Within this theory, the Kirchhoff stress **T**, is chosen as a suitable measure of the stress state and the stress–strain relation in the rate form is expressed as

$$\overset{\triangledown}{\mathbf{T}} = \boldsymbol{L}^{\boldsymbol{e}}(\boldsymbol{D} - \mathbf{D}^{\mathbf{p}}) \tag{1}$$

where the Jaumann derivative of the Kirchhoff stress, $\overset{\triangledown}{\mathbf{T}}$, is given as

$$\overset{\triangledown}{\mathbf{T}} = \dot{\mathbf{T}} - \mathbf{W}\mathbf{T} + \mathbf{T}\mathbf{W} \tag{2}$$

$\dot{\mathbf{T}}$ is the material derivative of the Kirchhoff stress and **W** the total (crystal) spin tensor. To simplify the calculation, the fourth-order elasticity tensor, $\boldsymbol{L}^{\boldsymbol{e}}$, is taken in the present work to be equal to the one for the linear isotropic materials in the form

$$\boldsymbol{L}^{\boldsymbol{e}} = 2G\left(\boldsymbol{I} - \frac{1}{3}\mathbf{I} \otimes \mathbf{I}\right) + B(\mathbf{I} \otimes \mathbf{I}) \tag{3}$$

where ***I*** is the fourth-order identity tensor, **I** the second-order identity tensor, G the elastic shear modulus and B the elastic bulk modulus. **D** and $\mathbf{D}^{\mathbf{p}}$ in Equation 1 are the total stretching tensor and the plastic stretching tensor, respectively.

The plastic stretching tensor, $\mathbf{D}^{\mathbf{p}}$, as defined by the crystalline plasticity theory (e.g. [12]) is given by

$$\mathbf{D}^{\mathbf{p}} = \sum_{\alpha=1}^{K} \dot{\gamma}^{\alpha}\mathbf{R}^{\alpha} \tag{4}$$

where $\dot{\gamma}^{\alpha}$ is the shear strain rate associated with slip system α, and K is the total number of slip systems, and the symmetric traceless Schmid tensor, $\mathbf{R}^{\alpha}$, is defined as

$$\mathbf{R}^{\alpha} = \frac{1}{2}\{\mathbf{s}^{\alpha} \otimes \mathbf{n}^{\alpha} + \mathbf{n}^{\alpha} \otimes \mathbf{s}^{\alpha}\} \tag{5}$$

where $\mathbf{s}^{\alpha}$ and $\mathbf{n}^{\alpha}$ are, respectively, the slip direction and the slip plane normal corresponding to slip system α.

The shear strain rate associated with slip system α is given as

$$\dot{\gamma}^{\alpha} = \dot{\gamma}_0^{\alpha}\frac{\tau^{\alpha}}{g^{\alpha}}\left|\frac{\tau^{\alpha}}{g^{\alpha}}\right|^{\mathrm{m}^{\alpha}-1} \tag{6}$$

where $\dot{\gamma}_0^{\alpha}$ is the reference shear strain rate, m^{α} the rate exponent (inverse of the shear rate sensitivity coefficient) and g^{α} the strength of slip system α. The resolved shear stress on slip system α, τ^{α}, is given as

$$\tau^{\alpha} = \mathbf{T}' \times \mathbf{R}^{\alpha} \tag{7}$$

where $\mathbf{T}'$ is the deviatoric part of the Kirchhoff stress.

The slip system strength, g^α, evolves with deformation as

$$g^\alpha = g_0^\alpha + \int_0^t \dot{g}^\alpha \mathrm{d}t \tag{8}$$

where g_0^α is the initial slip system strength and t the time. The hardening rate, $\dot{g}^\alpha$, is defined as

$$\dot{g}^\alpha = \sum_{\beta=1}^{K} h^{\alpha\beta} |\dot{\gamma}^\beta| \tag{9}$$

where $h^{\alpha\beta}$ is the hardening modulus whose components show the effect of shear on slip system β on the strength of slip system α.

Substitution of Equations 5 and 6 into Equation 4 yields

$$\mathbf{D^p} = \sum_{\alpha=1}^{K} \left(\dot{\gamma}_0^\alpha \frac{\mathbf{T}' \times \mathbf{R}^\alpha}{g^\alpha} \left| \frac{\mathbf{T}' \times \mathbf{R}^\alpha}{g^\alpha} \right|^{\mathrm{m}^\alpha - 1} \right) \mathbf{R}^\alpha \tag{10}$$

Using the relation $(\mathbf{A} \times \mathbf{B})\mathbf{C} = (\mathbf{C} \otimes \mathbf{A})\,\mathbf{B}$, where **A**, **B** and **C** are all second-order tensors, Equation 10 can be rewritten as

$$\mathbf{D^p} = \sum_{\alpha=1}^{K} \left(\dot{\gamma}_0^\alpha \frac{1}{g^\alpha} \left| \frac{\mathbf{T}' \times \mathbf{R}^\alpha}{g^\alpha} \right|^{\mathrm{m}^\alpha - 1} \mathbf{R}^\alpha \otimes \mathbf{R}^\alpha \right) \mathbf{T}' \tag{11}$$

The total (crystal) spin, **W**, can be additively decomposed as the sum of plastic spin, $\mathbf{W^p}$, and the lattice spin, $\mathbf{W}^*$ [13] as

$$\mathbf{W} = \mathbf{W^p} + \mathbf{W}^* \tag{12}$$

In accordance with the crystal plasticity theory (e.g. [12]), the plastic spin is given as

$$\mathbf{W^p} = \sum_{\alpha=1}^{K} \dot{\gamma}^\alpha \mathbf{A}^\alpha \tag{13}$$

where $\mathbf{A}^\alpha$ is the skew part of the Schmid tensor associated with slip system α and is defined as

$$\mathbf{A}^\alpha = \frac{1}{2}\{\mathbf{s}^\alpha \otimes \mathbf{n}^\alpha - \mathbf{n}^\alpha \otimes \mathbf{s}^\alpha\} \tag{14}$$

The lattice spin causes rotation of the crystal lattice. Following Asaro and Rice [13], the rate of the change of the orientation of crystal lattice can be expressed as

$$\dot{\mathbf{C}} = \mathbf{W}^*\mathbf{C} \tag{15}$$

where **C** is the lattice orientation matrix given as

$$\mathbf{C} = \begin{bmatrix} \cos\psi\cos\phi - \sin\psi\cos\theta\sin\phi & \sin\psi\cos\phi + \cos\psi\cos\theta\sin\phi & \sin\theta\sin\phi \\ -\cos\psi\sin\phi - \sin\psi\cos\theta\cos\phi & -\sin\psi\sin\phi + \cos\psi\cos\theta\cos\phi & \sin\theta\cos\phi \\ \sin\psi\sin\theta & -\cos\psi\sin\theta & \cos\theta \end{bmatrix} \tag{16}$$

with ψ, θ and ϕ being the Euler angles relating the global co-ordinate system and the one defined by the crystal axes.

2.1.1. Matrix material

As discussed earlier, the alloys studies in the present work consist of the matrix (composed of parallel lamellae of γ-TiAl and α_2-Ti_3Al) and dispersed particles of the beta phase. A finite element analysis of polycrystalline material consisting of parallel γ-TiAl and α_2-Ti_3Al lamellae as the matrix and dispersed beta phase in the form of particles requires the use of a sufficiently fine mesh. A three-dimensional finite element analysis of this material would entail prohibitively large amounts of computer memory and computer processing unit (CPU) time and, consequently, in the present work, only a two-dimensional idealization of this problem, analogous to that developed by Kad *et al.* [14], is pursued.

As stated earlier, the matrix consists of parallel γ-TiAl and α_2-Ti_3Al lamellae with the orientation relationship: $(0\,0\,0\,1)_{\alpha_2} \| \{1\,1\,1\}_\gamma$ and $\langle 1\,1\,\bar{2}\,0\rangle_{\alpha_2} \| \langle 1\,\bar{1}\,0\rangle_\gamma$ and the lamellae interface $(0\,0\,0\,1)_{\alpha_2} \| \{1\,1\,1\}_\gamma$. In the two-dimensional plane strain finite element analysis carried out in the present work, the three-dimensional crystal slip is replaced by its two-dimensional projection onto the $(1\,\bar{2}\,1)_\gamma \| \{1\,0\,1\,0\}_{\alpha_2}$ plane. As shown by Kad *et al.* [14], such in-plane slip is controlled by three slip systems: (a) the projected $\langle 1\,\bar{1}\,0](1\,1\,1)_\gamma$ slip system, which is characterized by a relatively small initial value of the slip strength ($g_0^\alpha = 40$–60 MPa); and (b) and (c) two projected $(1\,1\,\bar{2}\,1)[1\,1\,\bar{2}\,6]_{\alpha_2}$ pyramidal slip systems, which are substantially harder ($g_0^\alpha = 500$–700 MPa). As shown in Fig. 1a, the slip directions corresponding to these three slip systems designated as s_1, s_2, and s_3 form an isosceles triangle with an angle $\phi = 58^\circ$ between the soft and the hard slip systems.

To simplify the computation, the matrix has been treated as a single phase, consisting of a continuum mixture of γ and α_2 (the continuum composite approximation), but its plastic behaviour is taken to be controlled by the $\langle 1\,\bar{1}\,0](1\,1\,1)$ slip in γ-TiAl (slip system 1) and by two projected $(1\,1\,\bar{2}\,1)[1\,1\,\bar{2}\,6]$ slip systems of α_2-Ti_3Al (slip systems 2 and 3). The initial slip strengths are set to the following values: $g_0^1 = 50$ MPa, $g_0^2 = g_0^3 = 600$ MPa. These values are consistent with the lamellar γ-TiAl + α_2-Ti_3Al material, having an average grain size of 100 μm and a lamellar thickness of 2.5 μm. The hardening is taken to be linear and the effect of the latent hardening is neglected ($h_{ij} = 0, i \neq j$). Following Kad *et al.* [14] the non-zero elements of the hardening matrix, h_{ij}, are set as follows: $h_{11} = 150$ MPa and $h_{22} = h_{33} = 1500$ MPa. Furthermore, the slip system parameters $\dot{\gamma}_0^\alpha$ and m^α defined in Equation 6, are set as 1×10^{-3} and 11, respectively.

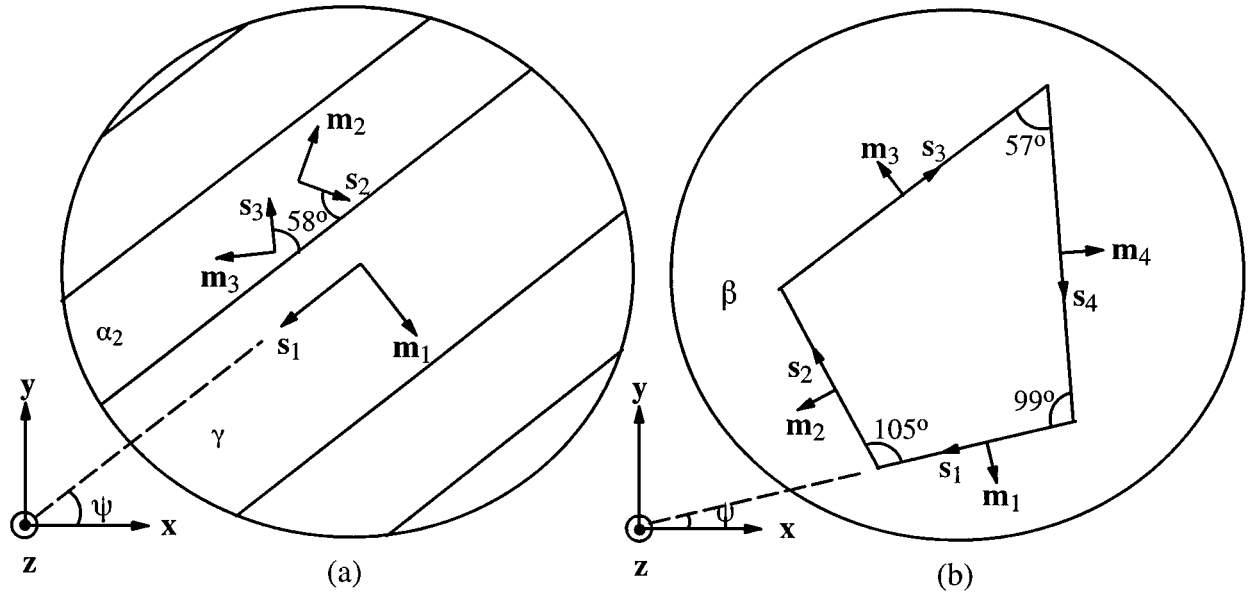

Figure 1 The projected slip systems used in the two-dimensional finite element analysis of (a) the γ-TiAl plus α_2-Ti_3Al matrix, and (b) beta phase precipitates.

2.1.2. Dispersed phase

2.1.2.1. Stable beta phase. The stable beta phase dispersed in the form of fine particles has b.c.c. crystal structure in which slip occurs in $\langle 1\,1\,1\rangle$ directions on $\{1\,1\,0\}$, $\{1\,1\,2\}$ and $\{1\,2\,3\}$ planes. The in-plane slip in this phase is simplified as follows: The four $\langle 1\,1\,1\rangle$ directions are projected on an arbitrary plane associated with the [0 0 1] zone axis resulting in four slip systems $\mathbf{s}_1$, $\mathbf{s}_2$, $\mathbf{s}_3$ and $\mathbf{s}_4$. The Miller indices of this plane (7 3 0) are generated using the random number generator. The angles between these four slip systems, given in Fig. 1b, are kept fixed for all beta phase particles. However, the orientation of each particle is made different by selecting the Euler angle, ψ, in a random fashion. Following Grujicic and Sankaran [5, 6] the parameters appearing in the constitutive model of the stable beta phase are chosen as: $\dot{\gamma}_0^\alpha = 1 \times 10^{-3}$, $m^\alpha = 11$, $g_0^\alpha = 85$ MPa, $h_{ii}^\alpha = 1500$ MPa and $h_{ij}^\alpha = 0$ (for $i \neq j$).

2.1.2.2. Metastable beta phase. The metastable beta phase undergoes a b.c.c. $\rightarrow$ hexagonal close packed (h.c.p.) martensitic transformation under stress. According to Burgers [15], the b.c.c. $\rightarrow$ h.c.p. martensitic transformation can be described in terms of two elemental processes: (a) shuffling of parallel adjacent $(1\,1\,0)$ planes in the opposite $[1\,1\,0]$ direction, and (b) pure shear on the $\{1\,1\,2\}$ planes in the $\langle 1\,1\,1\rangle$ direction. The shuffling produces the required h.c.p.-type ABAB stacking of the close packed $(0\,0\,0\,1)_{\text{h.c.p.}}$ planes and causes a volume change, but does not give rise to shear. The transformation shear, on other hand, converts the irregular hexagonal atomic arrangement in the $(1\,1\,0)_{\text{b.c.c.}}$ planes into regular hexagonal atomic arrangement in the close packed $(0\,0\,0\,1)_{\text{h.c.p.}}$ planes. Since for the b.c.c. $\rightarrow$ h.c.p. transformation to take place both shuffling and pure shear have to occur, and the shear directions $\langle 1\,1\,1\rangle$ are the same as those for slip, the b.c.c. $\rightarrow$ h.c.p. transformation is modelled in the present work as crystal slip, which produces not only shear but also dilation. This was done as follows: First, it is recognized that the plastic stretching tensor defined in Equations 4, 10 or 11 is, in fact, purely deviatoric ($\mathbf{D}^{\mathbf{p}\prime}$). Due to the aforementioned coupling between the transformation shear and the transformation shuffling, the hydrostatic part of the plastic stretching, $\mathbf{D}_\mathbf{h}^\mathbf{p}$, is defined as

$$\mathbf{D}_\mathbf{h}^\mathbf{p} = f(\bar{\varepsilon}^\mathrm{p})\left(\frac{2}{3}\mathbf{D}^{\mathbf{p}\prime} \times \mathbf{D}^{\mathbf{p}\prime}\right)^{1/2} \mathbf{I} \tag{17}$$

where the function $f(\bar{\varepsilon}^\mathrm{p})$, as defined by Grujicic and Sankaran [5, 6], takes into account the fact that martensitic transformation initially dominates plastic behaviour, while at larger levels of equivalent plastic strain, $\bar{\varepsilon}^\mathrm{p}$, the crystal slip becomes the dominant mode of deformation. According to Grujicic and Sankaran [5, 6], for the Ti–V–Al based beta phase, the function $f(\bar{\varepsilon}^\mathrm{p})$ can be defined as

$$f(\bar{\varepsilon}^\mathrm{p}) = \begin{cases} 15.105\bar{\varepsilon}^{\mathrm{p}2} - 1.550\bar{\varepsilon}^\mathrm{p} + 0.040 & \bar{\varepsilon}^\mathrm{p} \leq 0.048 \\ 0 & \bar{\varepsilon}^\mathrm{p} > 0.048 \end{cases} \tag{18}$$

In order to account for dynamic softening, which dominates transformation in its early stages, and static hardening, which dominates transformation in its later stages, the elements of the hardening matrix are defined as [5, 6]

$$h_{ii}^\alpha(\bar{\gamma}^\alpha) = -16\,180.349\bar{\gamma}^{\alpha^3} + 2586.213\bar{\gamma}^{\alpha^2} - 89.884\bar{\gamma}^\alpha - 1.802\,(\times 10^9) \tag{19a}$$

and

$$h_{ij}^\alpha(\bar{\gamma}^\alpha) = 0 \qquad \text{for } i \neq j \tag{19b}$$

where $\bar{\gamma}^{\alpha}$ is the accumulated shear strain associated with slip system α.

Following Grujicic and Sankaran [5, 6], the remaining parameters appearing in the constitutive relations for the metastable beta phase are set as: $g_0^{\alpha} = 75\,\text{MPa}$ $\dot{\gamma}_0^{\alpha} = 1 \times 10^{-3}$ and $\text{m}^{\alpha} = 11$.

The uniaxial stress–strain behaviour of the metastable and the stable beta phase as well as that of the matrix phase obtained using the constitutive relations developed in this section is shown and discussed in Section 3.

2.2. Grain boundary–interface constitutive relations

2.2.1. Cohesive zone model

The matrix grain boundary and precipitate–matrix interfaces have been modelled using the cohesive zone framework originally introduced by Needleman [9]. The cohesive zone is assumed to have a negligible thickness when compared with other characteristic lengths of the problem, such as the grain boundary–interface edge length, typical lengths associated with the gradient of the fields, etc. The mechanical behaviour of the cohesive zone is characterized by a traction–displacement relation, which is introduced through the definition of an interface potential, Ψ. Stable equilibrium for the grain boundary–interface corresponds to a perfectly bonded configuration, where the potential has a minimum and all tractions vanish. For any other configuration, the value of the potential is taken to depend only on the displacement jump across the interface. For the two-dimensional problem at hand, the interface displacement jump is expressed in terms of its normal component, U_{n}, and a tangential component, U_{t}, where both components lie in the x–y plane of the Cartesian co-ordinate system.

Differentiating the interface potential function $\Psi = \hat{\Psi}(U_{\text{n}}, U_{\text{t}})$ with respect to U_{n} and U_{t} yields, respectively, the normal and tangential components of F, the traction per unit grain boundary–interface area in the deformed configuration

$$F_{\text{n}}(U_{\text{n}}, U_{\text{t}}) = \frac{-\partial \hat{\Psi}(U_{\text{n}}, U_{\text{t}})}{\partial U_{\text{n}}} \tag{20}$$

$$F_{\text{t}}(U_{\text{n}}, U_{\text{t}}) = \frac{-\partial \hat{\Psi}(U_{\text{n}}, U_{\text{t}})}{\partial U_{\text{t}}} \tag{21}$$

The interface constitutive relations are thus fully defined by specifying the form for the interface potential function $\hat{\Psi}(U_{\text{n}}, U_{\text{t}})$.

The interface potential of the following form initially proposed by Socrate [16], is used in the present study

$$\hat{\Psi}(U_{\text{n}}, U_{\text{t}}) = \left\{ -\text{e}\sigma_{\max}\delta_{\text{n}} + \frac{1}{2}\tau_{\max}\delta_{\text{t}} \log\left[\cosh\left(2\frac{U_{\text{t}}}{\delta_{\text{t}}}\right)\right]\right\}\left[\text{e}^{-\frac{U_{\text{n}}}{\delta_{\text{n}}}}\left(1 + \frac{U_{\text{n}}}{\delta_{\text{n}}}\right)\right] \tag{22}$$

where the parameters $\sigma_{\max}$ and $\tau_{\max}$ are, respectively, the normal and tangential interfacial strengths, and δ_{n} and δ_{t} are the corresponding characteristic interface lengths. Differentiation of Equation 22 with respect to U_{n} and U_{t} yields the expressions for the interfacial tractions

$$F_{\text{n}}(U_{\text{n}}, U_{\text{t}}) = \left\{ e\sigma_{\max} - \frac{1}{2}\tau_{\max}\frac{\delta_{\text{t}}}{\delta_{\text{n}}} \log\left[\cosh\left(2\frac{U_{\text{t}}}{\delta_{\text{t}}}\right)\right]\right\}\left(\frac{U_{\text{n}}}{\delta_{\text{n}}}\text{e}^{-\frac{U_{\text{n}}}{\delta_{\text{n}}}}\right) \tag{23}$$

$$F_{\text{t}}(U_{\text{n}}, U_{\text{t}}) = \left[\tau_{\max}\tanh\left(2\frac{U_{\text{t}}}{\delta_{\text{t}}}\right)\right]\left[\text{e}^{-\frac{U_{\text{n}}}{\delta_{\text{n}}}}\left(1 + \frac{U_{\text{n}}}{\delta_{\text{t}}}\right)\right] \tag{24}$$

Graphical representation of the two functions defined by Equations 23 and 24 is given in Fig. 2.

If F_{n} given by Equation 23 is expressed for the case of purely normal interface decohesion, and the F_{t} for the case of pure sliding, one obtains

$$F_{\text{n}}(U_{\text{n}}, U_{\text{t}} = 0) = F_{\text{n}}^{0}(U_{\text{n}}) = \text{e}\sigma_{\max}\left(\frac{U_{\text{n}}}{\delta_{\text{n}}}\text{e}^{-\frac{U_{\text{n}}}{\delta_{\text{n}}}}\right) \tag{25}$$

$$F_{\text{t}}(U_{\text{n}} = 0, U_{\text{t}}) = F_{\text{t}}^{0}(U_{\text{t}}) = \tau_{\max}\tanh\left(2\frac{U_{\text{t}}}{\delta_{\text{t}}}\right) \tag{26}$$

Inspection of Equations 25 and 26 shows that the grain boundary–interface behaviour is characterized by four parameters: $\sigma_{\max}$, δ_{n}, $\tau_{\max}$ and δ_{t}; where $\sigma_{\max}$ is the

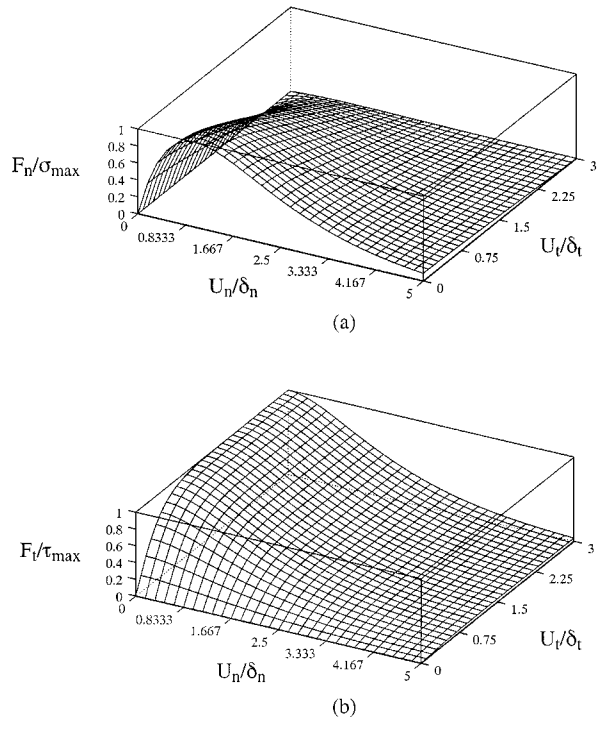

Figure 2 Normal and tangential components of the traction per unit interface area, as a function of the normalized normal, $U_{\text{n}}/\delta_{\text{n}}$, and tangential, $U_{\text{t}}/\delta_{\text{t}}$, components of the interface displacements.

peak normal traction for purely normal interface decohesion; δ_n as the normal interface separation; which corresponds to this peak traction; τ_{max} as an asymptotic shear traction for interface sliding; and δ_t as a characteristic length in pure sliding, which corresponds to a shear traction within 1% $\tau_{max}(F_t^0(\delta_t) \simeq 0.99\,\tau_{max})$. These four parameters are determined in the present work as a function of the grain–grain and grain–precipitate misorientation and the grain boundary–interface orientation using a molecular statics approach, which is described in the next section.

2.2.2. Atomic-scale analysis of grain boundaries and interfaces

Because γ-TiAl is the dominant phase in the matrix material, the atomic simulation analysis is applied to the gamma–gamma grain boundaries and gamma–beta interfaces. To analyse any particular grain boundary or interface, a gamma–gamma or gamma–beta atomistic bicrystal is first constructed with the corresponding orientations of the two crystals and the boundary–interface separating the crystals. An example of the gamma–beta atomistic crystal is given in Fig. 3. The edge lengths of the single crystals are expressed in terms of the number of interplanar spacings $d_{(u\,v\,w)}$ of the $(u\ v\ w)$ planes. The atomic interactions are accounted for through the use of the embedded atom method (EAM) interatomic potential [17]. These potentials for the Ti–Al–V system at hand have been derived and extensively tested by Grujicic and Dang [18, 19].

Prior to forming the bicrystals, the equilibrium lattice parameters at 0 K in each phase are determined by carrying out the potential energy minimization (the molecular static method) in each single crystal through the use of the conjugate gradient method [20]. For the $L1_0$ TiAl gamma phase, the following lattice parameters are obtained: $a_\gamma = 0.3944$ nm and $c_\gamma = 0.4010$ nm, resulting in a c_γ/a_γ ratio of 1.05, which is in fair agreement with its experimental counterpart $c_\gamma/a_\gamma = 1.03$ [21].

The beta phase with 15 at % V is chosen in the present work because it was found previously [2] that at this level of vanadium, the b.c.c. structure is generally stable and can undergo martensitic transformation only in the presence of high stress, such as the one encountered in the vicinity of a sharp crack. For the Ti–15V b.c.c. phase, the energy minimization procedure yielded the lattice parameter $a_\beta = 0.3186$ nm, which is in reasonable agreement with its experimental counterpart (0.322 nm) [22].

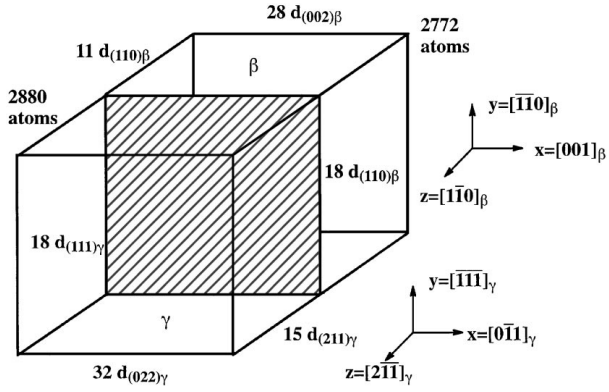

Figure 3 Schematic representation of the beta/gamma bicrystal used for determination of the $(1\,1\,0)_\beta/(2\,1\,1)_\gamma$ interfacial decohesion potential.

2.2.2.1. Computation of grain boundary–interface structure. The equilibrium structure of the grain boundaries and interfaces at 0 K is determined by minimizing the potential energy of each bicrystals using the conjugate gradient method under flexible periodic boundary conditions in two directions parallel to the interface and the free surface boundary conditions in the direction normal to the interface. The use of the free surface boundary conditions allows the spacing of the planes parallel to and near the interface to adjust to the differences in the atomic environment. The equilibrium atomistic configuration for the gamma–beta interface corresponding to the bicrystal, given in Fig. 3, is shown in Fig. 4. As indicated in Fig. 4c, the interface structure can be described in terms of two arrays of parallel dislocations marked D1 and D2. The Burger's vector for the two arrays has been determined as $b_{D1} = 0.5a_\beta[0\,0\,1]_\beta$, $b_{D2} = 0.086a_\beta[7\,7\,6]_\beta$, and the corresponding dislocation spacing $\lambda_{D1} = 3.5a_\beta$ and $\lambda_{D2} = 1.81a_\beta$.

2.2.2.2. Computation of interface–grain boundary decohesion potential. The interface decohesion potential for each of the four bicrystals is determined by first rigidly displacing the two single crystals in each case in normal and tangential directions by different amounts. The potential energy of the bicrystals is next minimized under the constraint that the average displacements of the atoms in the interface planes in each of the two joined crystals remain equal to the imposed rigid–body displacements. The difference between the energies of the bicrystal in the displaced configuration and in the equilibrium configuration expressed per unit area of the grain boundary–interface is then defined as the value of the grain boundary–interface decohesion potential, Ψ, at the given values of U_n and U_t.

For the gamma–beta interface shown in Fig. 4 and for the normal separation in the $[\bar{2}\,1\,1]_\gamma \| [\bar{1}\,1\,0]_\beta$ direction and tangential displacement in the $[0\,1\,1]_\gamma \| [0\,0\,1]_\beta$ direction, the following interfacial parameters are obtained: $\sigma_{max} = 7.29$ GPa, $\delta_n = 0.09$ nm, $\tau_{max} = 1.20$ GPa and $\delta_t = 0.33$ nm. It should be noted that due to the periodic nature of the interface structure, atomistic simulation analysis predicts a periodic interface potential relative to the tangential displacements. To comply with the form of the interface potential given by Equation 22, only the portion of the atomistic simulation results that show an increase of F_t with U_t is used and fitted using Equation 22.

2.3. Polycrystalline finite element method

2.3.1. Finite element mesh

To analyse the polycrystalline behaviour of the material at hand, a finite element mesh consisting of 971 quadrilateral and 364 triangular elements is used in the present work and is shown Fig. 5a. The mesh is partitioned into 27 equiaxed (hexagonal) matrix grains, Fig. 5b, and 27

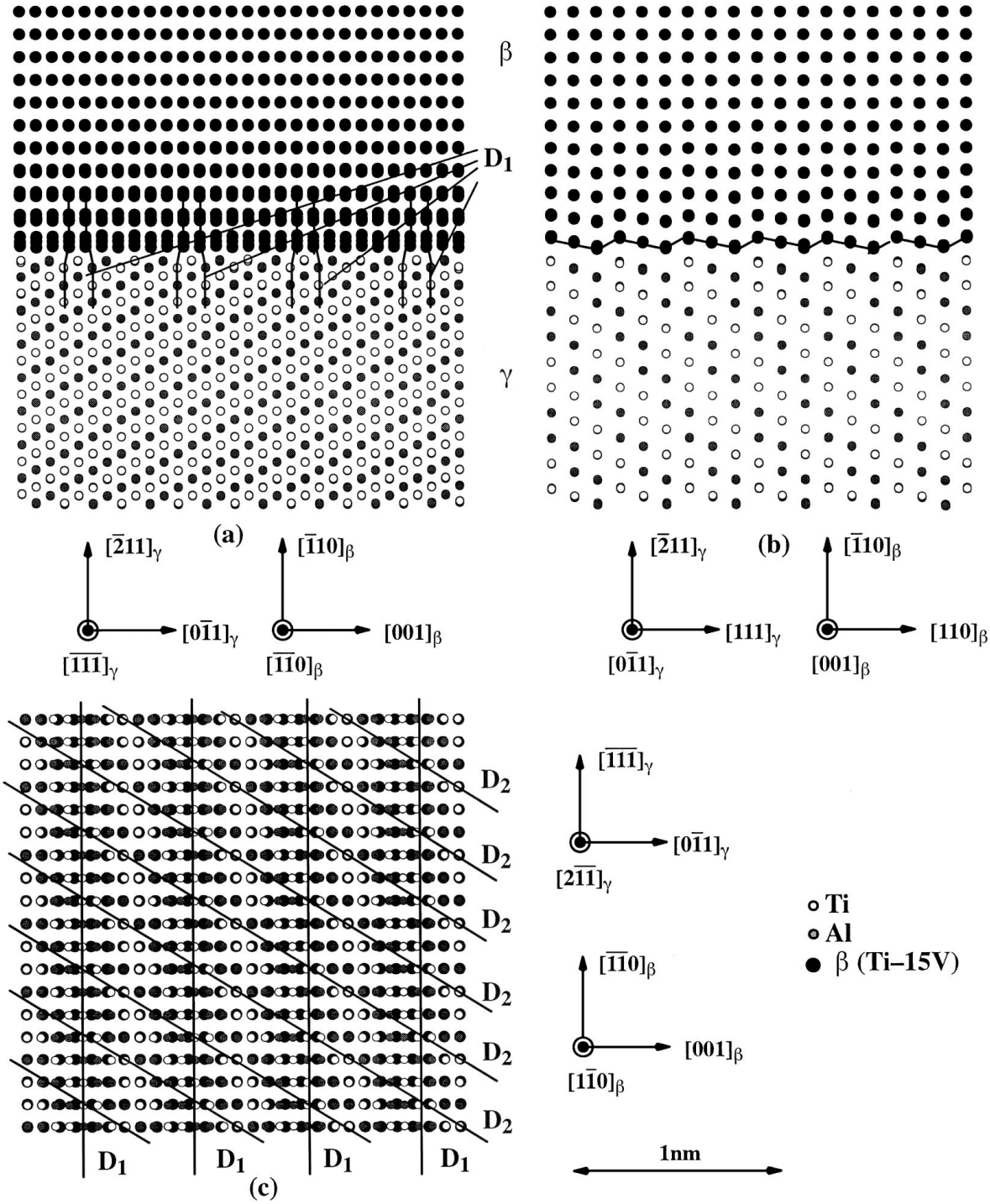

Figure 4 Equilibrium configuration of the $(1\,\bar{1}\,0)_\beta/(2\,\bar{1}\,\bar{1})_\gamma$ interface: (a) atomic positions projected onto the $(\bar{1}\,\bar{1}\,0)_\beta/(\bar{1}\,\bar{1}\,\bar{1})_\gamma$ plane, (b) atomic positions projected onto the $(0\,\bar{0}\,\bar{1})_\beta/(0\,\bar{1}\,1)_\gamma$ plane, and (c) atomic positions projected onto the $(1\,1\,0)_\beta/(2\,\bar{1}\,\bar{1})_\gamma$ interface plane. Interfacial dislocations are marked as D_1 and D_2.

matrix grains and 56 equiaxed (hexagonal) precipitates located at matrix–three-grain junctions, Fig. 5c. The configuration shown in Fig. 5c corresponds to approximately 10 vol % of the precipitate phase. As discussed in the previous section, the matrix grain boundaries and the matrix–precipitate phase interfaces are modelled using the cohesive zone approach. The initial orientation (the Euler angle, ψ, in degrees) of the matrix grains and the beta phase precipitates is indicated in Fig. 5b and c. The grain numbers and precipitate numbers are also indicated in Fig. 5b and c, respectively. The initial (reference) configuration is assumed to be stress free and not to contain any lattice perturbations. The two-phase polycrystalline aggregates defined in Fig. 5b and c are loaded in the *y*-direction, while constraining the four straight edges of the aggregates to remain straight and parallel to their original orientation with no strain being allowed in the *z*-direction. While the aggregates possess no special symmetry and are not expected to deform in the enforced orthotropic manner, each aggregate is treated here as a "material point" and according to the Taylor assumption its deformation gradient is assumed to be equal to the global deformation gradient.

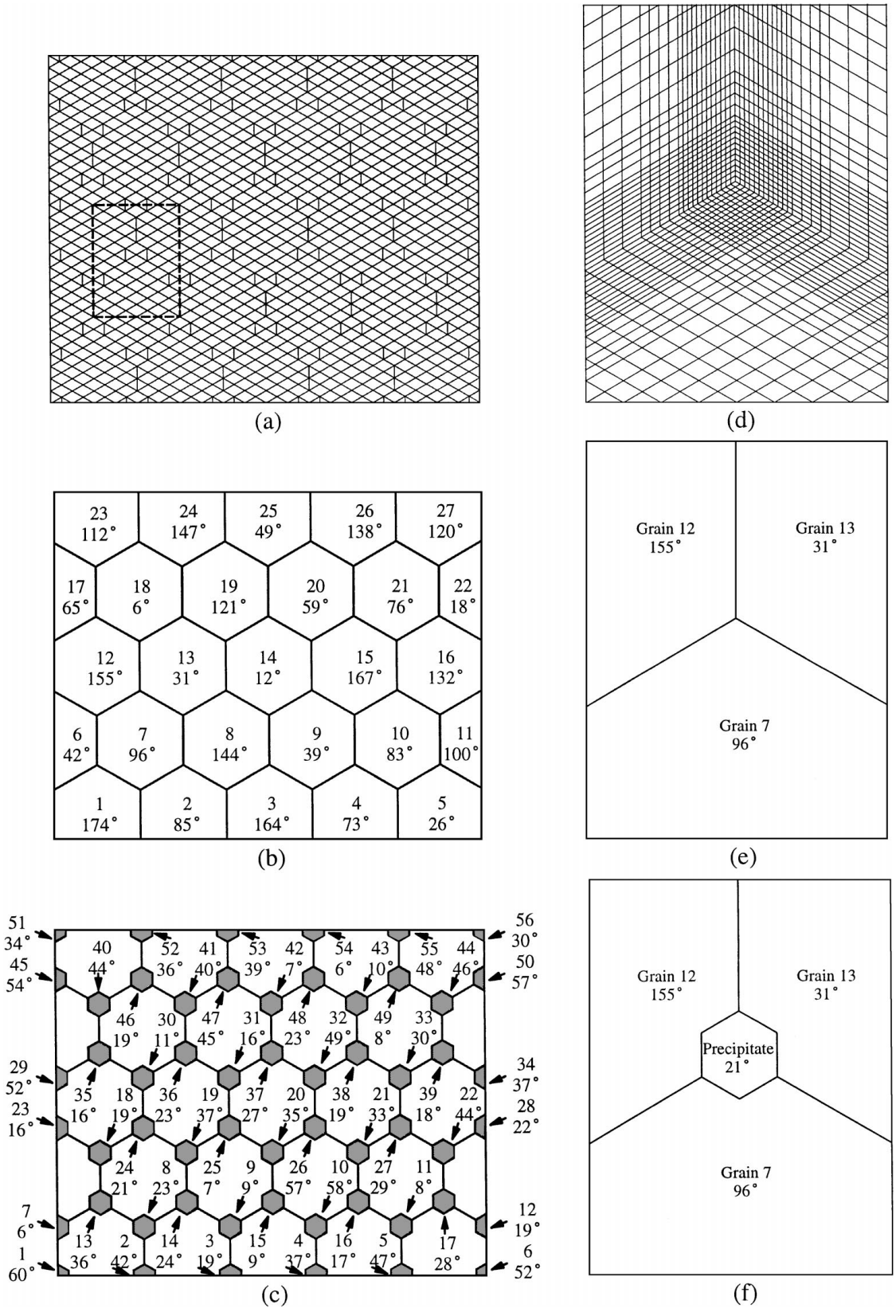

Figure 5 (a) The finite element mesh consisting of 971 quadrilateral and 364 triangular elements, (b) the polycrystalline reference configuration consisting of 27 matrix grains and (c) of 27 matrix grains and 56 precipitates located at three-grain junctions (the numbers represent the grain number and the magnitude of the grain's Euler angle in degrees), (d) the finite element mesh consisting of 1338 quadrilateral and 28 triangular elements, and (e) the polycrystalline reference configuration consisting of three matrix grains and (f) of three matrix grains with a precipitate located at the three-grain junction. The rectangular region marked in (a) corresponds to the region shown in (d)–(f).

Based on the results obtained for the two–phase polycrystalline aggregate, the rectangular region marked using dashed lines in Fig. 5a is selected for further study. This region is divided into 1338 quadrilateral and 28 triangular elements, Fig. 5d, and partitioned either into three matrix grains, Fig. 5e, or into three matrix grains and one precipitate, Fig. 5f. The loading in this case is applied by assigning the displacement history to the

boundary of the aggregates shown in Fig. 5e and f to be identical to that of the corresponding rectangular region marked in Fig. 5a.

2.3.2. Implementation into the finite element method code ABAQUS

2.3.2.1. Integration of material state. The materials constitutive model defined in Section 2.1 has been incorporated into the finite element method (FEM) code ABAQUS [8]. This code gives the user the flexibility of specifying a constitutive law through a "user material" subroutine, UMAT. The user is provided with the values of the stress and all user-defined state variables at the beginning of the time step. The increment in total strain is also provided as an estimate of the kinematic solution. The user must update the stress tensor and the state variables based on this estimate. In addition, when a boundary value problem is being solved using the finite element method, a knowledge of the material Jacobian for each Gaussian integration point at each time step is required to evaluate the element's stiffness matrix, the user must also evaluate the material Jacobian. Evaluation of the material Jacobian for the present constitutive model by a numerical integration of the material state is briefly discussed in this section.

If the Kirchhoff stress tensor at time, t (the beginning of a time step) is $\mathbf{T_0}$, the updated stress tensor at a new time, $t + \Delta t$ (the end of the time step), is then given by

$$\mathbf{T} = \mathbf{T_0} + \Delta\mathbf{T} \tag{27}$$

The increment in stress, $\Delta\mathbf{T}$, can be defined as the integral of the Jaumann stress rate tensor and is given by

$$\Delta\mathbf{T} = \int_t^{t+\Delta t} \overset{\triangledown}{\mathbf{T}}\,\mathrm{d}t \tag{28}$$

Equation 28 can be evaluated numerically using the generalized trapezoidal rule

$$\Delta\mathbf{T} = \eta\overset{\triangledown}{\mathbf{T}}\Delta t + (1-\eta)\overset{\triangledown}{\mathbf{T}_0}\Delta t \qquad (0 \le \eta \le 1) \tag{29}$$

In the present work η was set to one, which reduces the trapezoidal rule to the Euler backwards difference method.

By combining Equations 27, 28 and 1, the updated stress tensor is now expressed as

$$\mathbf{T} = \mathbf{T_0} + \Delta t\boldsymbol{L}^{\boldsymbol{e}}(\mathbf{D}) - \Delta t\boldsymbol{L}^{\boldsymbol{e}}(\mathbf{D^p}) \tag{30}$$

After introducing the total strain increment, $\Delta\varepsilon$

$$\Delta\varepsilon = \mathbf{D}\Delta t \tag{31}$$

Equation 30 can be rewritten as

$$\mathbf{T} = \mathbf{T_0} + \boldsymbol{L}^{\boldsymbol{e}}\Delta\varepsilon - \Delta t\boldsymbol{L}^{\boldsymbol{e}}(\mathbf{D^p}) \tag{32}$$

Since both the stress tensor at the beginning of time step, $\mathbf{T_0}$, and the total strain increment for the time step, $\Delta\varepsilon$, are known, the first two terms on the right-hand side of Equation 32 are known. The third term can be obtained by multiplying Equation 11 by $\Delta t\boldsymbol{L}^{\boldsymbol{e}}$.

Combining Equations 32 and 11, and taking advantage of the fact that $\mathbf{R}^\alpha$ is traceless, and hence $\mathbf{T_h} \times \mathbf{R} = \mathbf{0}$, where $\mathbf{T_h}$ is the hydrostatic stress tensor ($\mathbf{T} = \mathbf{T_h} + \mathbf{T}'$), yields

$$\mathbf{T} = \mathbf{T_0} + \boldsymbol{L}^{\boldsymbol{e}}\left[\Delta\varepsilon - \Delta t\sum_{\alpha=1}^{K}\left(\dot{\gamma}_0^\alpha\frac{1}{g^\alpha}\left|\frac{\mathbf{T}\times\mathbf{R}^\alpha}{g^\alpha}\right|^{\mathrm{m}^\alpha-1}\mathbf{R}^\alpha\otimes\mathbf{R}^\alpha\right)\mathbf{T}\right] \tag{33}$$

If $\mathbf{R}^\alpha$ and g^α are taken to be equal to their values at the beginning of the time step, Equation 33 represents a system of six non-linear algebraic equations with six unknown Kirchhoff stress components. In the present work, this system of equations was solved using the IMSL subroutine, HYBRJ [23].

Once the stress components are calculated, the plastic stretching, $\mathbf{D^p}$, the plastic spin, $\mathbf{W^p}$ and the increments in plastic strain tensor, $\Delta\varepsilon^{\mathrm{p}}$, can be evaluated using Equations 11, 13 and 31, respectively.

For the case of the metastable beta phase, Equation 33 is expressed in terms of deviatoric stresses and deviatoric strain and solved. Next, Equation 17 is used to evaluate the hydrostatic part of plastic stretching, and the stress updated using the relations

$$\mathbf{T} = \mathbf{T_0} + \boldsymbol{L}^{\boldsymbol{e}}\left[\Delta\varepsilon - \Delta t\left(\mathbf{D}^{\mathbf{p}\prime} + \mathbf{D}_{\mathbf{h}}^{\mathbf{p}}\right)\right] \tag{34}$$

Next the slip system strength, g^α, and the lattice orientation matrix are updated as follows. Equation 8 is replaced with its Euler backwards differencing equivalent

$$g^\alpha = g_0^\alpha + \dot{g}^\alpha\Delta t \tag{35}$$

where $\dot{g}^\alpha$ can be expressed by combining Equations 6, 7 and 9

$$\dot{g}^\alpha = \sum_{\beta=1}^{K} h^{\alpha\beta}\dot{\gamma}_0^\beta\left|\frac{\mathbf{T}\times\mathbf{R}^\beta}{g^\beta}\right|^{\mathrm{m}^\beta} \tag{36}$$

After combining Equations 35 and 36, one obtains a system of K non-linear algebraic equations with K unknown g^αs, which is readily solved using the subroutine HYBRJ [23].

The lattice orientation matrix, $\mathbf{C}$, is updated by integrating Equation 15 to yield

$$\mathbf{C} = \exp(\mathbf{W}^*\Delta t)\mathbf{C_0} \tag{37}$$

where $\mathbf{C}$ and $\mathbf{C_0}$ are the lattice orientation matrices at the end and the beginning of the time step, respectively. The lattice spin, $\mathbf{W}^*$, is determined by subtracting from the total crystal spin, $\mathbf{W}$ (passed into the UMAT subroutine) the plastic spin, $\mathbf{W^p}$.

2.3.2.2. Computation of material Jacobian. The material Jacobian, $\boldsymbol{J}$, is a fourth-order tensor that represents the rate of change in the increment of the Kirchhoff stress, $\Delta\mathbf{T}$, with respect to a virtual change in the increment in strain, $\Delta\varepsilon$. Thus

$$\boldsymbol{J} = \frac{\mathbf{d}\Delta\mathbf{T}}{\mathbf{d}\Delta\varepsilon} \tag{38}$$

Using Equation 16 and the fact that $\mathbf{T_0}$ is a constant for the current time increment and using Equation 27, the material Jacobian can be written as

$$\boldsymbol{J} = \frac{\mathbf{dT}}{\mathbf{d}\Delta\varepsilon} \tag{39}$$

Substitution of Equation 33 into Equation 39 yields

$$\boldsymbol{J} = \frac{\mathbf{d}}{\mathbf{d}\Delta\varepsilon}\left\{\mathbf{T_0} + \boldsymbol{L^e}\left[\Delta\varepsilon - \Delta t \sum_{\alpha=1}^{K}\left(\dot{\gamma}_0^{\alpha}\frac{1}{g^{\alpha}}\left|\frac{\mathbf{T}\times\mathbf{R}^{\alpha}}{g^{\alpha}}\right|^{m^{\alpha}-1}\mathbf{R}^{\alpha}\otimes\mathbf{R}^{\alpha}\right)\mathbf{T}\right]\right\} \tag{40}$$

The differentiation indicated in Equation 40 is carried out using the component representation of the stress and the strain increment. The procedure is straightforward; however, the final expression for the material Jacobian components are very lengthy and are not given here. A detailed derivation of the material Jacobian is given by Zhang [24].

2.3.2.3. Derivation of the interface element stiffness matrix. The grain boundary–interface decohesion potentials developed in Section 2.2 are incorporated into the UEL subroutine of ABAQUS to define the stiffness matrix of the interfacial elements. The UEL subroutine allows the user to define the contribution of the interfacial (continuum) elements to the global finite element model. In other words, for the given nodal displacements of the interface elements provided to UEL by ABAQUS, the contribution of the interfacial elements to the global vector of residual forces and to the global Jacobian (element stiffness matrix) is determined in the UEL subroutine and passed to ABAQUS. The implementation of the interface decohesion potential in the UEL subroutine is discussed below.

Each interface element is defined as a four-node isoparametric element on the gamma–gamma grain boundary or the beta–gamma interface S, as shown schematically in Fig. 6. In the undeformed configuration (not shown for brevity), nodes 1 and 4, and nodes 2 and 3 coincide, respectively. A local co-ordinate system, consistent with directions that are tangent (t) and normal (n) to the interface, is next assigned to the each element. This is done by introducing two "internal nodes", A and B, located at the midpoints of the lines 1–2 and 3–4, connecting the corresponding grain boundary–interface nodes of the two grains.

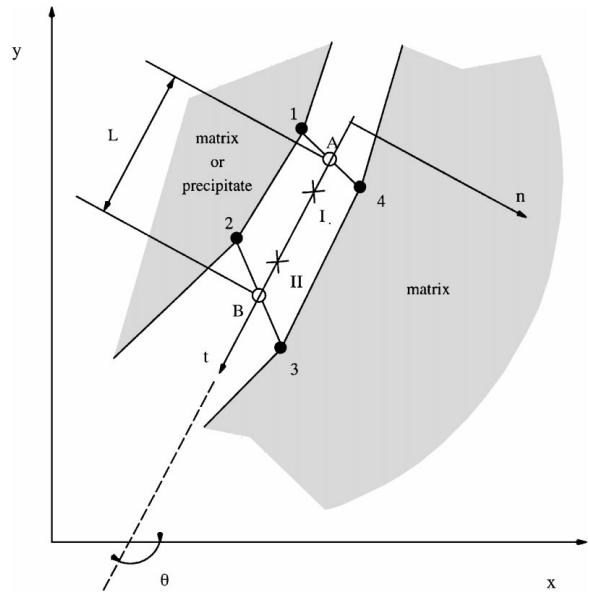

Figure 6 Definition of the linear, four-node interface element. Nodes 1 and 4 and nodes 2 and 3 coincide in the equilibrium (reference) configuration. Internal nodes A and B located at the midpoints of segments connected corresponding nodes in the beta and gamma sides of the interface, two integration points marked as + and a local t–n co-ordinate system are also indicated.

The interface displacements at the internal nodes A and B are expressed in terms of the displacements of the element nodes 1–4

$$U_{\mathrm{n}}^{\mathrm{A}} = \left(U_y^4 - U_y^1\right)\cos\theta - \left(U_x^4 - U_x^1\right)\sin\theta \tag{41a}$$

$$U_{\mathrm{t}}^{\mathrm{A}} = \left(U_y^4 - U_y^1\right)\sin\theta - \left(U_x^4 - U_x^1\right)\cos\theta \tag{41b}$$

$$U_{\mathrm{n}}^{\mathrm{B}} = \left(U_y^3 - U_y^2\right)\cos\theta - \left(U_x^3 - U_x^2\right)\sin\theta \tag{41c}$$

$$U_{\mathrm{t}}^{\mathrm{B}} = \left(U_y^3 - U_y^2\right)\sin\theta - \left(U_x^3 - U_x^2\right)\cos\theta \tag{41d}$$

An isoparametric co-ordinate, η, is next introduced along the tangent direction with $\eta(\mathrm{A}) = -1$ and $\eta(\mathrm{B}) = 1$ and two linear Langrangian interpolation functions are defined as $\mathrm{N_A}(\eta) = (1-\eta)/2$ and $\mathrm{N_B}(\eta) = (1+\eta)/2$.

The interpolation functions given above allow the normal and the tangential components of the interface displacements to be expressed in the form of their values at the internal nodes A and B

$$U_{\mathrm{n}}(\eta) = N_{\mathrm{A}}(\eta)U_{\mathrm{n}}^{\mathrm{A}} + \mathrm{N_B}(\eta)U_{\mathrm{n}}^{\mathrm{B}} \tag{42a}$$

$$U_{\mathrm{n}}(\eta) = N_{\mathrm{A}}(\eta)U_{\mathrm{n}}^{\mathrm{A}} + \mathrm{N_B}(\eta)U_{\mathrm{n}}^{\mathrm{B}} \tag{42b}$$

The tangential and normal components of the forces at modes A and B, i.e. $F_{\mathrm{t}}^{\mathrm{A}}$, $F_{\mathrm{t}}^{\mathrm{B}}$, $F_{\mathrm{n}}^{\mathrm{A}}$, $F_{\mathrm{n}}^{\mathrm{B}}$, which are work conjugates of the corresponding nodal displacements $U_{\mathrm{t}}^{\mathrm{A}}$, $U_{\mathrm{t}}^{\mathrm{B}}$, $U_{\mathrm{n}}^{\mathrm{A}}$ and $U_{\mathrm{n}}^{\mathrm{B}}$, are next determined through the application of virtual work to the interfacial element

$$\int_{-1}^{1}\delta\Phi(\eta)L\,\mathrm{d}\eta = \sum_{\mathrm{I}=\mathrm{n,t}}\sum_{\mathrm{N}=\mathrm{A,B}} F_{\mathrm{I}}^{\mathrm{N}}\delta U_{\mathrm{I}}^{\mathrm{N}} \tag{43}$$

where L is the A–B element length. The perturbation of interface potential is expressed in terms of the

perturbations of the interface displacements at the internal nodes A and B, U_t^A, U_t^B, U_n^A and U_n^B

$$\delta\Phi = \frac{\partial\Phi[U_t(\eta), U_n(\eta)]}{\partial U_n}\left[N_A(\eta)\partial U_n^A + N_B(\eta)\partial U_n^B\right] + \frac{\partial\Phi[U_t(\eta), U_n(\eta)]}{\partial U_t}\left[N_A(\eta)\partial U_t^A + N_B(\eta)\partial U_t^B\right] \quad (44)$$

By substituting Equation 44 into Equation 43 and by choosing one of the δU_l^N (N = A, B; l = t, n) perturbations at a time to be unity and the remaining perturbations to be zero, the corresponding F_l^N component of the nodal force can be expressed as

$$F_I^N = \int_{-1}^{1} \frac{\partial\Phi[U_t(\eta), U_n(\eta)]}{\partial U_I} N_N(\eta) L \, d\eta \quad (45)$$

Using a straightforward geometrical procedure and imposing the equilibrium condition, the corresponding residual nodal forces R_x^i and R_y^i ($i = 1$–4) in the global x–y co-ordinate system, are defined as

$$R_x^1 = -R_x^4 = F_t^A \cos\theta - F_n^A \sin\theta \quad (46a)$$

$$R_y^1 = -R_y^4 = F_t^A \sin\theta - F_n^A \cos\theta \quad (46b)$$

$$R_x^2 = -R_x^3 = F_t^B \cos\theta - F_n^B \sin\theta \quad (46c)$$

$$R_y^2 = -R_y^3 = F_t^B \sin\theta + F_n^B \cos\theta \quad (46d)$$

The components of the element Jacobian are next defined as

$$\frac{\partial R_j^i}{\partial U_l^k} = \sum_{I=n,t}\sum_{N=A,B}\sum_{j=n,t}\sum_{M=A,B} \frac{\partial R_j^i \partial F_I^N \partial U_J^M}{\partial F_I^N \partial U_J^M \partial U_l^k} \quad (47)$$

where the components of the internal Jacobian $\partial F_i^N / \partial U_j^M$ (i, j = n, t; N, M = A, B) are calculated by differentiation of Equation 45. The residual nodal forces given by Equation 46 and the element Jacobian given by Equation 47 are computed in the UEL subroutine, and passed to ABAQUS for use in its global Newton scheme for accurate assessment of kinematics.

3. Results and discussion

3.1. Polycrystalline tensile stress–strain relations

3.1.1. Single phase materials

In this section, the polycrystalline tensile stress–strain behaviour of the matrix phase and the stable and the metastable forms of the beta phase are determined. Toward that end, the matrix phase and constitutive properties of the stable and the metastable beta phase materials discussed in Sections 2.1.1 and 2.1.2, are, in turn, assigned to the 27-grain configuration shown in Fig. 5b. In this set of calculations, the grain boundaries are modelled as rigid. The configuration is stretched in the y-direction and the plane-strain condition applied in the z-direction. As discussed in Section 2.3.1, orthotropic-type constrains are also imposed in the x–y plane in order to preserve the rectangular shape of the configuration.

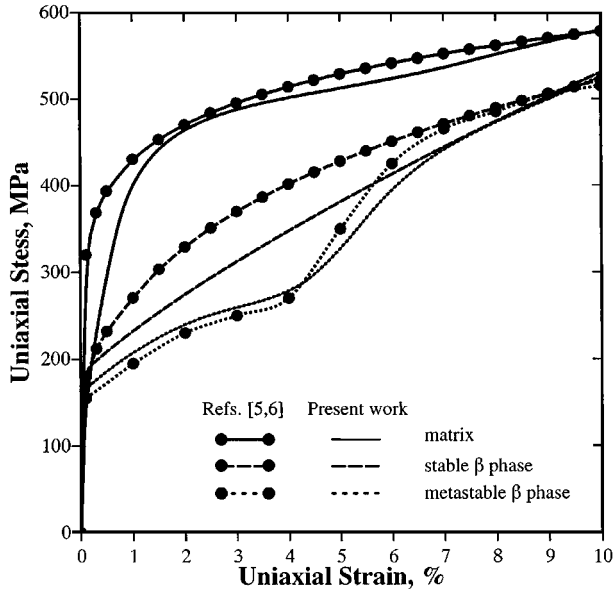

Figure 7 Comparison of the uniaxial (plane-strain) stress–strain behaviour for the metastable and stable beta phase and for the matrix phase calculated in the present work and measured by Grujicic and Sankaran [5, 6].

The resulting uniaxial (plane-strain) stress–strain curves for the three cases are shown in Fig. 7. For comparison the corresponding experimental results reported by Grujicic and Sankaran [5, 6] are also included. The agreement between the two sets of results can be considered as reasonable. The results shown in Fig. 7 also clearly display the characteristic features of the three materials, such as:

1. The matrix phase has a relatively high value of yield stress (approximately 400 MPa), but strain hardens relatively slowly.
2. The stable beta phase has a flow stress (approximately 200 MPa) that is approximately half of that of the matrix phase, but strain hardens at a significantly higher rate.
3. The metastable beta phase has an even lower initial yield stress (approximately 160 MPa) and initially strain hardens very slowly (the dynamic softening region dominated by the high rate of martensitic transformation acts as a deformation process). At the intermediate levels of plastic strain, the hardening rate of the metastable phase increases (the static hardening region governed by higher flow stress levels of the transformation product – martensite). At the later stages of deformation when the transformation is near completion, the stress–strain curve for the metastable beta phase approaches that for the stable beta phase.

3.1.2. Two phase materials

In this section, a polycrystalline aggregate consisting of 27 matrix grains and 56 precipitates, Fig. 5c is used to determine the plane-strain stress–strain relations for materials consisting of 10 vol % of the stable or the metastable beta phase precipitates. The type of loading

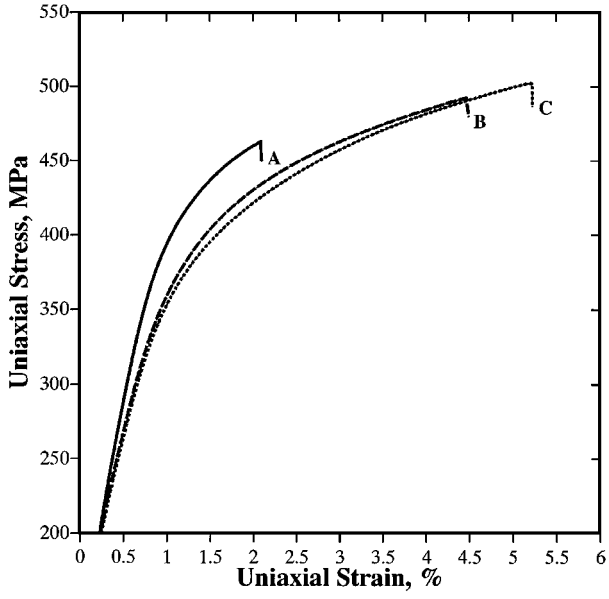

Figure 8 The computed uniaxial stress–strain (plane-strain) relations using cohesive zone approximation: (A) matrix phase, (C) matrix phase plus stable beta phase precipitate, (D) matrix phase plus metastable beta phase precipitate.

and orthotropic constraints used in the previous section are also utilized in this section. However, the grain boundaries and phase interfaces are modelled using the cohesive zone approach. The results of this calculation are shown in Fig. 8. Curve B pertains to the case of the stable beta phase precipitates, whereas curve C pertains to the case of the metastable beta phase precipitates. For comparison, the stress–strain curve for the single (matrix) phase material is also shown in Fig. 8, Curve A.

The results shown in Fig. 8 show that the single phase material, Curve A, is harder than the two two-phase materials, but fails at a relatively small tensile strain of approximately 2.1%. The presence of stable beta phase precipitates increases the strain to fracture to approximately 4.5%, while the strain to fracture is approximately 5.2% for the case of metastable beta phase precipitates. Dynamic softening causes Curve C to lie below Curve B at lower strain values. However, due to the interplay of static hardening, the material containing metastable beta phase precipitates hardens faster at later stages of deformation.

3.2. Deformation fields

3.2.1. Multigrain length scale

3.2.1.1. Single phase material. In this section, the deformation fields are shown and discussed for either the 27-grain single-phase aggregate, Fig. 5b, or for the 27-grain plus 56-precipitate two-phase aggregate, Fig. 5c, loaded in plane-strain tension. Specifically, the contour plots are shown for:

1. The normal equivalent plastic strain;
2. The change in the Euler angle, ψ, which is a measure of two-dimensional lattice rotation; and
3. hydrostatic stress.

The distributions of the equivalent plastic strain, the change in the Euler angle and the hydrostatic stress for the single-phase material at an overall axial strain of 2% are shown in Fig. 9a–c, respectively. The contour plot given in Fig. 9a clearly shows a non-uniform distribution of the equivalent plastic strain. Furthermore, the localization of the strain into deformation bands at approximately $\pm 40^\circ$ is apparent as indicated by the arrows in Fig. 9a. The deformation bands were observed at an overall strain of approximately 0.5% (the contour plot is not shown for brevity) and they become more pronounced as deformation proceeds.

In addition to non-uniformity in the distribution of the equivalent plastic strain in the single-phase material at the 27-grain configuration level, the distribution of the equivalent strain is quite non-uniform within the grains (single crystals) too. For example, within grains 1, 10, 12 and 15 at the overall plastic strain of 2%, Fig. 9a, the strain varies between 1 and 7%. High gradients in the equivalent plastic strain are particularly pronounced in the regions near the grain boundaries (e.g. grain boundaries associated with grains 7 and 12 and grains 7 and 13) and near the three-grain junctions (e.g. 7–12–13 and 10–15–16 grain junctions).

The distribution of the change in Euler angle for the single-phase material at an overall plastic strain of 2% is shown in Fig. 9b. Counterclockwise lattice rotations are described as positive. A careful examination of Fig. 9b reveals that the largest rotations take place near the grain boundaries (e.g. the ones between grains 12 and 13, and grains 13 and 18) and near the three-grain junctions (e.g. 4–9–10, 5–10–11, 6–7–12, 7–12–13, 12–13–18, 13–18–19, 16–21–22, 17–18–23, 19–20–25 and 21–26–27 three-grain junctions). Furthermore, a comparison of the corresponding results shown in Fig. 9a and 9b suggests that the largest rotations take place within the grains located in the deformation bands (e.g. grains 2, 15 and 22, and grains 6, 13, 25 and 26). This is not surprising since the lattice rotations are a natural consequence of the effect of constraints imposed by the boundary conditions and the surrounding grains on crystallographic shear within a crystal. Hence, the regions characterized by the largest levels of equivalent plastic strain are generally expected to experience large magnitudes of the lattice rotation.

The distribution of the hydrostatic stress in the single-phase material throughout the 27-grain configuration at an overall plastic strain of 2% is shown in Fig. 9c. This figure clearly shows that hydrostatic stress is distributed quite non-uniformly not only among the grains but also within the grains. Specifically, grains, 5, 7, 12 and 26 are subject to tensile (positive) hydrostatic stresses, while the remaining grains experience both tensile and compressive hydrostatic stresses. High magnitude hydrostatic stresses are generally concentrated near the grain boundaries or near the three-grain junctions. In particular, the three-grain junction associated with grains 7, 12 and 13 is characterized by a high gradient and large magnitudes of positive hydrostatic stress. A comparison of the results shown in Fig. 9c with the results shown in Fig. 9b suggests that the most probable cause for the observed high magnitude and high gradient of the

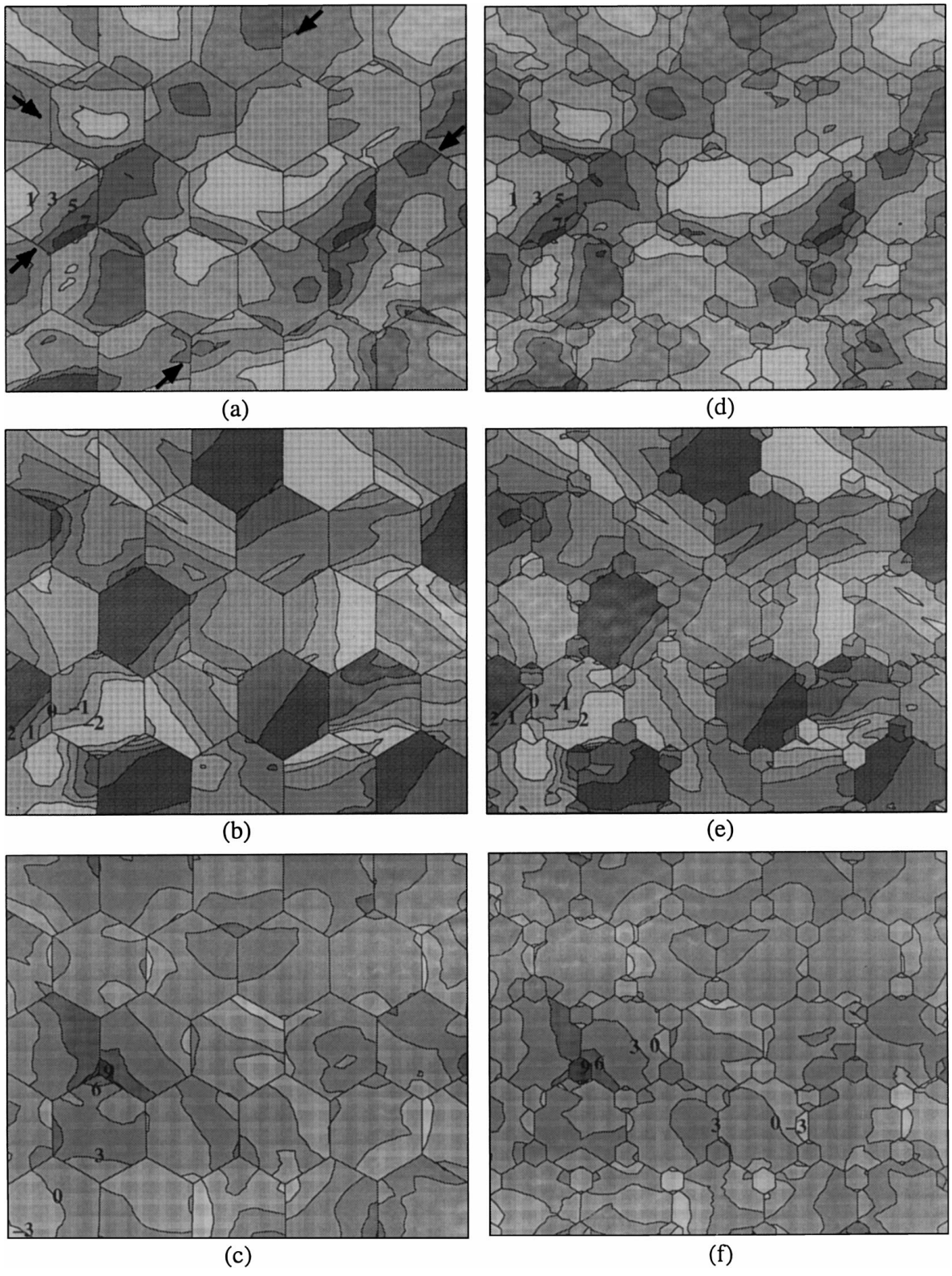

Figure 9 Contour plots at an overall normal strain of 2% in the vertical direction of: (a) the normal equivalent plastic strain (in per cent), (b) the changes in Euler angle (in degrees) and (c) the hydrostatic stress (in 100 MPa) for the single-phase (matrix) polycrystalline material in which the grain boundaries are represented using the cohesive zone model, and (d), (e) and (f) are the corresponding contour plots for the two-phase (matrix plus stable beta) material.

hydrostatic stress at the 7–12–13 three-grain junction is incompatibility in the plastic deformation of the three grains, which is manifested by a large variation in lattice rotations across the 7–13 and 12–13 grain boundaries. A similar conclusion can be drawn regarding the origin of the high hydrostatic stress region near the 19–20–25 three-grain junction. The concentration of hydrostatic stresses at the 10–15–16 three-grain junction, on the one hand, appears to be associated with a large concentration of the equivalent plastic strain in grain 15 near the 10–15 grain boundary. In this grain, the slip direction of the soft slip system (slip system 1, Fig. 1a is quite unfavourably oriented ($\psi = 167^\circ$) relative to the loading direction, which results in a small value of the

Schmid factor. Hence, a large stress in the loading direction is required for plastic deformation to take place within grain 15 and is due to incompatibility in the deformation of grains 10, 15 and 16 giving rise to large hydrostatic stress near the three-grain junction.

3.2.1.2. Two-phase material. The distributions of the equivalent plastic strain, the change in Euler angle and the hydrostatic stress for the material containing 10 vol % stable beta phase precipitates at an overall normal strain level of 2% are, respectively, shown in Fig. 9d–f. A comparison of the results shown in Fig. 9d–f with the corresponding results for the single-phase material, Fig. 9a–c, reveals the following:

1. Non-uniformity in the distribution of the equivalent palstic strain, Fig. 9d, is still present and, in fact, the deformation bands in the approximately 40° direction appear to be even more pronounced relative to the single-phase material case, Fig. 9a.
2. The variation in the change of Euler angle, ψ, Fig. 9e, is somewhat reduced in comparison with that shown in Fig. 9b. For example, within grain 13 the range of the Euler angle is between 0 and 2° in Fig. 9e, and between -2 and 2° in Fig. 9b.
3. The range of change in the Euler angle within the beta phase precipitates (e.g. precipitate 24) lies generally between the corresponding ranges of the surrounding grains (grains 7, 12 and 13). In this manner, the precipitates assist the accommodation of plastic flow incompatibilities between the adjacent grains.
4. The non-uniformity in the distribution of the hydrostatic stress, Fig. 9f, is generally similar to that in Fig. 9c. However, many precipitates (e.g. precipitates 24 and 27) are subject to a large tensile hydrostatic stress. This finding is consistent with the results shown in Fig. 9c, in which the regions around the three-grain junctions are generally characterized by a high level of hydrostatic stress. However, it should be noted that, while the precipitates themselves are subject to a high hydrostatic stress, in the matrix surrounding them the stress level has been substantially reduced. This implies that the normal tractions acting on the matrix grain boundaries and the precipitate–matrix interfaces are lowered, which, as will be shown in the next section, delays the onset of grain boundary–interface decohesion.

At the multigrain length scale for material containing 10 vol % metastable beta phase precipitates, the contour plots for the equivalent plastic strain, the change in Euler angle and the hydrostatic stress at an overall strain of 2% are very similar to the ones given in Fig. 9d–f and, hence, are not shown here. However, as will be shown in next section, at a single–grain length scale noticeable differences exist in the deformation fields between the two cases.

3.2.2. Single-grain length scale

In order to understand better the conditions leading to fracture by grain boundary decohesion and the mechanism by which beta phase precipitates increase the strain to fracture, the deformation fields within the 7–12–13 three-grain configuration, Fig. 5e, and the three-grain plus precipitate configuration, Fig. 5f, are examined in this section. As discussed in Section 2.3.2, the two configurations are loaded by prescribing the boundary displacements. These displacements are identical to the one obtained for the same regions in the 27-grain and 27-grain plus 56-precipitate aggregates, Fig. 5b, and c, respectively.

3.2.2.1. Single-phase material. The distributions of the equivalent plastic strain, the change in Euler angle and hydrostatic stress in the single-(matrix-) phase material at an overall strains of 1, 1.7 and 2.1% are shown in Fig. 10a–i. For improved clarity only the innermost hexagonal region centred at the three-grain junction is shown in this figure. The results shown in Fig. 10a–i, can be summarized as follows:

1. Well defined shear bands nearly parallel to the 7–12 grain boundary, characterized by large values of the equivalent strain, are obtained in grain 12 at 1% of the overall normal strain. Fig. 10a. These bands tend to broaden within grain 12 with further deformation. In addition, in the region within grain 13 near the 12–13 grain boundary, where the shear band of grain 12 impinges on this grain boundary, the equivalent plastic strain is quite large, Fig. 10 a–c. This is an indication of the way the non-uniformity of the plastic flow propagates from one grain to the next, resulting in formation of the macroscopic deformation bands observed in Fig. 9a.
2. At 1.7% of the overall strain, Fig. 10b, a small crack forms at the three-grain junction and extends slightly along the 12–13 and 7–13 grain boundaries. This reduces some of the constraints to the deformation of grain 7, causing it to undergo a large extent of plastic deformation in the region near the three-grain junction.
3. The distribution of the change in Euler angle within grian 12 has a band structure, Fig. 10d–e, in accordance with the shear bands shown in Fig. 10a–b.
4. Before nucleation of the crack at the three-grain junction, grain 7 undergoes positive lattice rotations in the region adjacent to the three-grain junction, Fig. 10d. However, when the crack forms, Fig. 10e, the part of grain 7 adjacent to the three-grain junction is less constrained and undergoes a negative lattice rotation.
5. Hydrostatic stress in grain 12 is also distributed in the form of bands parallel to the 7–12 grain boundary. Very large hydrostatic stresses are concentrated in the region surrounding the three-grain junction before grain boundary decohesion occurs, Fig. 10g. However, once the crack forms, the hydrostatic stresses undergo a major relaxtion, Fig. 10h versus g. As the crack advances, the region in the crack wake becomes subject to hydrostatic compression, Fig. 10i. The largest hydrostatic stresses generally remain ahead of the advancing crack, Fig. 10h and i.
6. Just prior to nucleation of the crack, the hydrostatic stress at the three-grain junction was found to

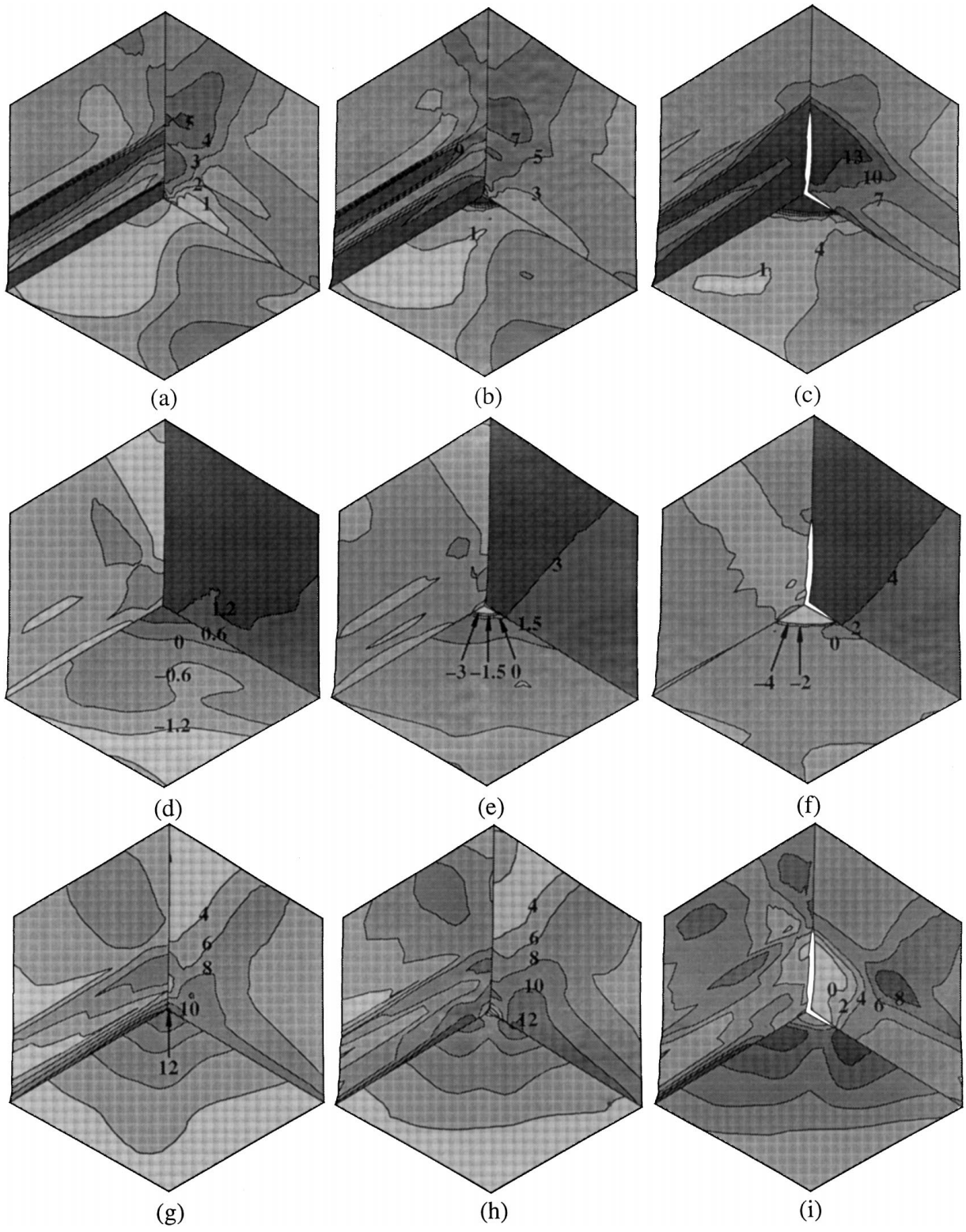

Figure 10 Contour plots for the normal equivalent plastic strain (in per cent) for the single-phase (matrix) material at overall normal strains of (a) 1, (b) 1.7 and (c) 2.1%. The corresponding contour plots for the change in Euler angle (in degrees) are shown in (d), (e) and (f). The corresponding contour plots for the hydrostatic stress (in 100 MPa) are shown in (g), (h) and (i).

reach a maximum value of 1.28 GPa. This value is comparable with the grain 7–grain 13 normal interface strength of 1.6 GPa.

3.2.2.2. Two-phase material containing stable beta phase precipitates. The distributions of the equivalent plastic strain, the change in Euler angle and hydrostatic stress in the configuration consisting of three grains and one precipitate of the stable beta phase. Fig. 5f, at overall strains of 1, 4.4 (the strain at which the crack nucleates) and 4.8% (the strain to fracture) are shown in Fig. 11a–i. The results can be summarized as:

1. The presence of beta phase precipitates does not lower the tendency for formation of shear bands in grain 12, Fig. 11a–c versus, Fig. 10a–c. In fact, the region containing the shear bands is somewhat larger in the two-phase material than in the single-phase material.

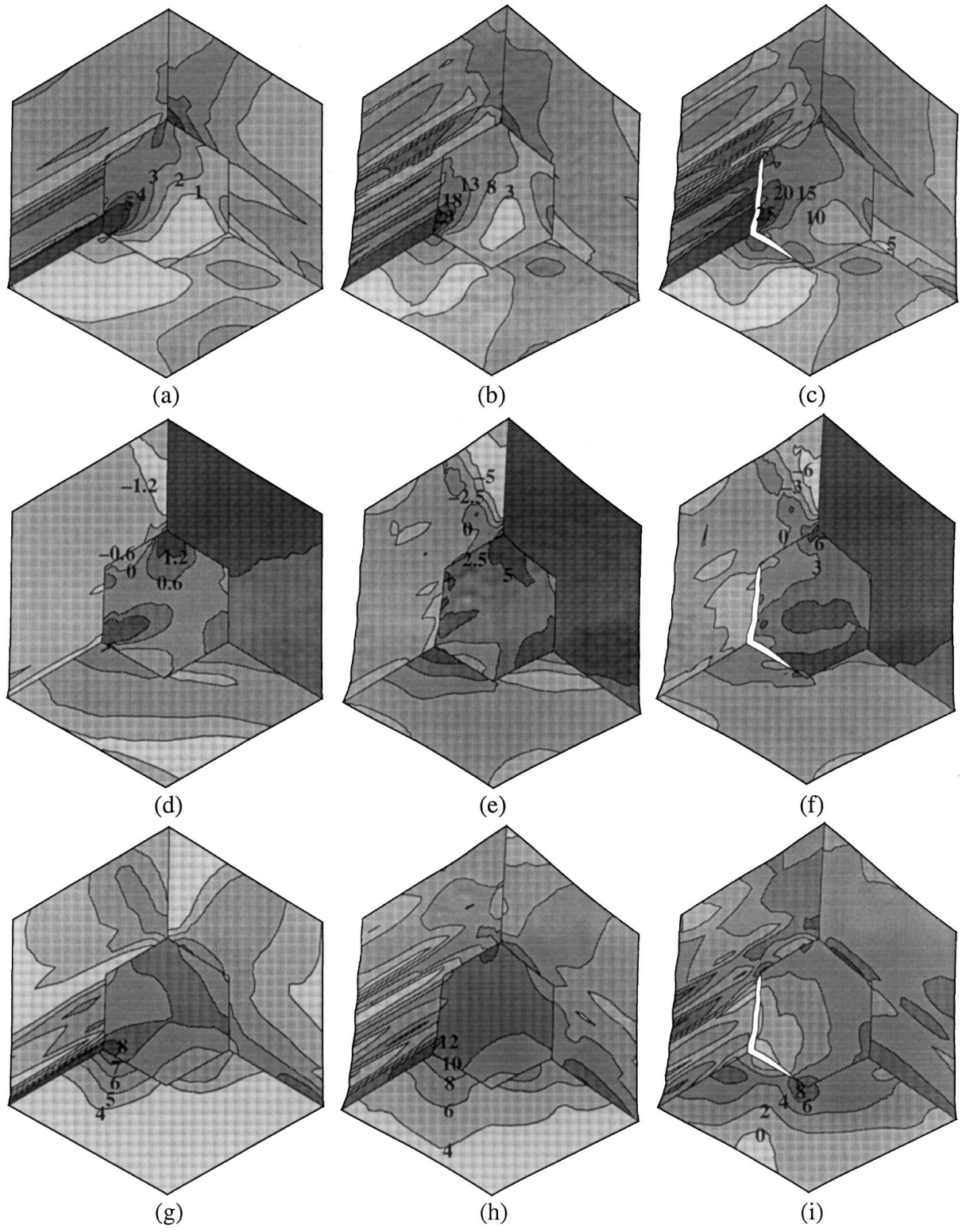

Figure 11 Contour plots for the normal equivalent plastic strain (in per cent) for the two-phase (matrix plus stable beta) material at overall normal strains of (a) 1, (b) 4.4 and (c) 4.8%. The corresponding contour plots for the change in Euler angle (in degrees) are shown in (d), (e) and (f). The corresponding contour plots for the hydrostatic stress (in 100 MPa) are shown in (g), (h) and (i).

2. The distribution of the equivalent plastic strain within the beta phase precipitate is quite non-uniform, but does not display shear band behaviour. The largest magnitudes of the equivalent plastic strain within the precipitate are found in the region near the grain 7–grain 12–precipitate junction.

3. The distribution in the change in Euler angle within grain 12 shows band structure, Fig. 11d–f, which is consistent with shear band structure, Fig. 11 a–c.

4. The change in Euler angle within the precipitate is quite non-uniform, with the largest gradient in the Euler angle change being located near the two grain–precipitate junction.

5. After a crack nucleates at the grain 7–grain 12–precipitate junction at an overall plastic strain of 4.4%, Fig. 11e, the precipitate becomes less constrained and the gradient in the change in Euler angle near this junction within the precipitate diminishes, Fig. 11f.

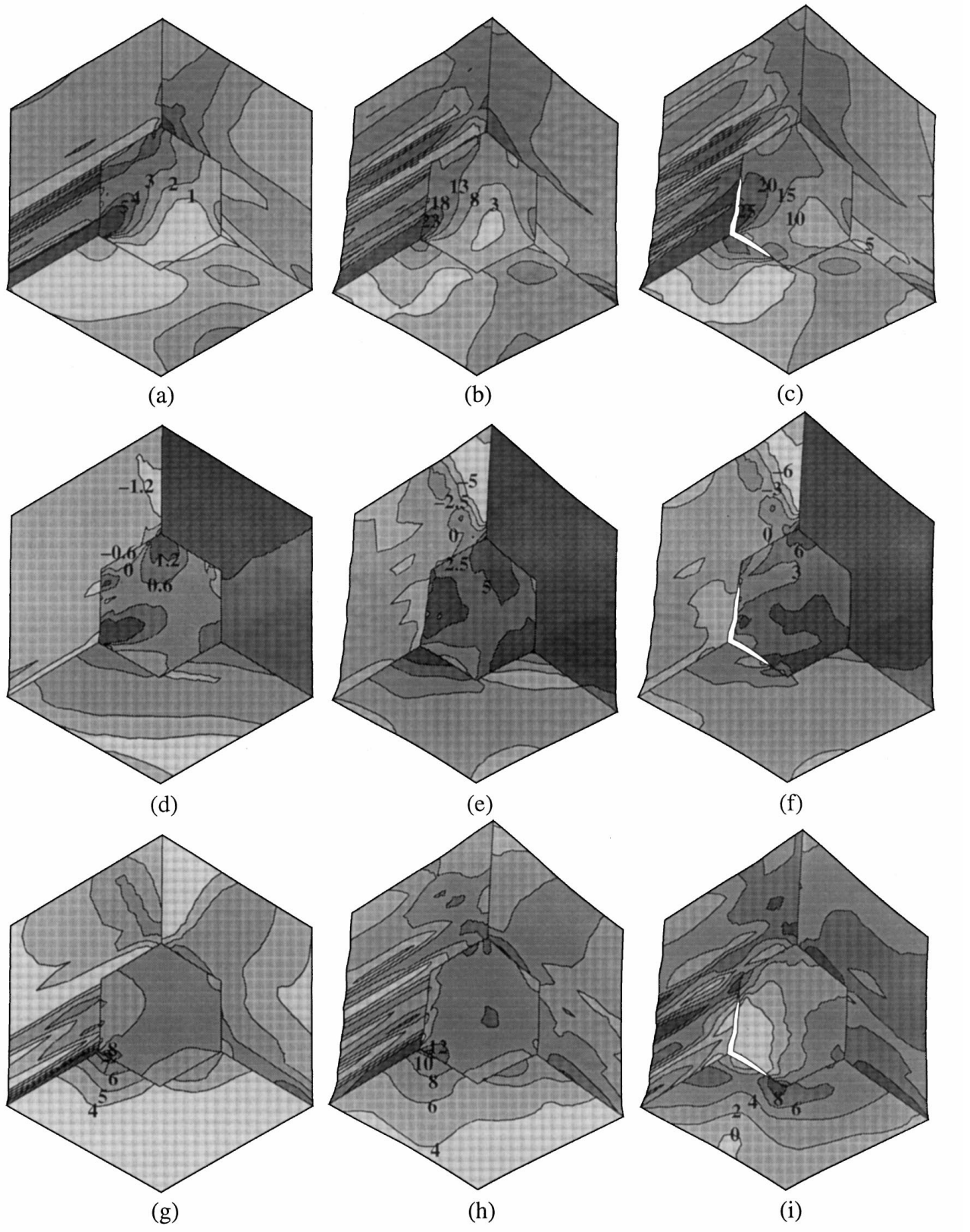

Figure 12 Contour plots for the normal equivalent plastic strain (in per cent) for the two-phase (matrix plus metastable beta) material at overall normal strains of (a) 1, (b) 4.8 and (c) 5.3%. The corresponding contour plots for the change in Euler angle (in degrees) are shown in (d), (e) and (f). The corresponding contour plots for the hydrostatic stress (in 100 MPa) are shown in (g), (h) and (i).

6. The presence of a precipitate generally lowers the magnitude of the hydrostatic stress relative to that in the single-phase material at the same level of overall plastic strain, Fig. 11g versus Fig. 10g.

7. The precipitate is generally subject to large positive hydrostatic stresses, with the largest values concentrated near the grain 7–grain 12–precipitate junction, Fig 11g. Upon nucleation of the crack, the level

of hydrostatic stress decreases sharply with the largest positive stresses now residing in the region in front of the crack tip, Fig. 11h, i. The regions in the crack wake undergo stress reversal and become subject to negative hydrostatic stress, Fig. 11i.

8. The peak value in hydrostatic stress, just prior to nucleation of the crack, was found to be 1.39 GPa, which is comparable with the grain 12–precipitate interface normal strength of 1.65 GPa.

9. The overall normal plastic increment between the nucleation point of the crack 4.4%, and final failure, 4.8%, is effectively the same as the corresponding range (1.7 and 2.1%) in the single-phase material.

3.2.2.3. Two-phase material containing metastable beta phase precipitates. The distributions of the equivalent plastic strain, the change in Euler angle and hydrostatic stress in the configuration consisting of three grains and one precipitate of the metastable beta phase, Fig. 5f, at overall strain ratios of 1, 4.8 (the strain at which the crack nucleates) and 5.3% (the strain to fracture) are shown, respectively, in Fig. 12a–i. A comparison of the these results with the ones shown in Fig. 11a–i, reveals the role of martensitic transformation as the deformation mechanism on the deformation fields and the onset of grain boundary–interface decohesion.

1. At the same level of overall strain, there is little difference in the distribution of the equivalent plastic strain, Fig. 12a versus Fig. 11a, and Fig. 12b versus Fig. 11c. As in the case of the configuration containing the stable beta phase precipitate, shear strain displays a pronounced deformation band behaviour in grain 12, which persists during deformation up to the onset of failure, Fig. 12a–c.

2. At an overall strain of 1%, the distribution of the change in Euler angle is very similar for the cases of the metastable and the stable beta phase precipitates, Fig. 12d versus Fig. 11d. However, at an overall strain of 4.8% of the distribution of the change in Euler angle is quite different in the two cases, Fig. 12e versus Fig. 11e. The reason for this difference is associated with the fact that in the case of the metastable beta phase precipitate the crack at the grain 7–grain 12–precipitate junction nucleates at an overall strain of 4.8%, the corresponding strain in the case of the stable beta phase precipitate is only 4.4%. Therefore, in the overall strain range between 4.4 and 4.8%, deformation of the grains and precipitate in the former case is more constrained than in the latter case. In fact, comparison of the change in Euler angle for the two cases at the moment of fracture, Figs 12f and 11f, shows similar qualitative features.

3. The largest difference between the two cases is seen when the distribution of the hydrostatic stress is considered. Even at an overall strain of 1%, the contour plots shown in Figs 11g and 12g are quite different. The most prominent difference is that in the case of the stable beta phase precipitate the largest positive hydrostatic stress is located near the grain 7–grain 12–precipitate junction, Fig. 11g. In sharp contrast, for the case of the metastable beta phase precipitate, the highest hydrostatic stress levels are found away from the aforementioned junction, Fig. 12g. This can be attributed to the fact that very extensive plastic deformation, which takes place in the region next to the junction, Fig. 12a, is dominated by the martensitic transformation, which is associated with lattice expansion, causing relaxation of the hydrostatic stress. This also explains why nucleation of the crack at the grain 7–grain 12–precipitate junction is delayed in the case of the metastable beta phase precipitate.

4. Nucleation of the crack is found to take place at a peak hydrostatic stress of 1.4 GPa, which is practically identical to that for the stable beta phase precipitate. This finding is reasonable since the same grain boundary and interface potentials are used for both the material containing a stable and the material containing a metastable beta phase precipitate.

5. The overall strain increment between crack nucleation and final behaviour ($5.3 - 4.8 = 0.5\%$) is somewhat larger than that for the case of the stable beta phase precipitate (0.4%).

4. Conclusions

Based on the results obtained in the present study the following main conclusions can be drawn:

1. Incompatibilities in plastic flow between adjacent grains can result in a large build-up tensile hydrostatic stress in the region surrounding certain three-grain junctions and, in turn, give rise to grain boundary cracking. While within the present model, grain boundary–interface decohesion is the only allowed mode of failure, the fact that the computed fracture strain (2.1%) is very comparable with its experimental counterparts (1.5–3.0%) suggests that grain boundary cracking plays an important role in fracture of the materials at hand. The observed intergranular fracture is consistent with the scanning electron microscopy results of Kad *et al.* [10], which show that while the fracture surface reveals a combination of intergranular and transgranular fracture modes, the region underneath the fracture surface contains numerous grain boundary cracks. In other words, fracture appears to be initiated by grain boundary decohesion with subsequent crack propagation taking place in a mixed mode. The present analysis, however, did not permit incorporation of the transgranular mode of fracture.

2. Incompatibilities in plastic flow between adjacent matrix grains are greatly reduced if beta phase precipitates are introduced at three-grain junctions. By virtue of their lower strength and a larger number of slip systems, the beta phase precipitates reduce the build-up in hydrostatic stress and, in turn, increase the strain to fracture.

3. An additional increase in fracture strain is obtained if the beta phase precipitates undergo a martensitic transformation. The beneficial effect of martensitic transformation is associated with accompanied lattice expansion, which further reduces the build-up in hydrostatic stress and delays the onset of grain boundary–interface decohesion.

Acknowledgements

This material is based upon work supported by the National Science Foundation under grants DMR-9317804 and CMS-9531930 and by the US Army Research Office under grant number DAAH04-96-1-0197. The authors are indebted to Drs Bruce A. MacDonald and William A. Spitzig of NSF and Dr Wilbur C. Simmons of ARO for their continuing interest in the present work. The authors also acknowledge the support of the office of High Performance Computing Facilities at Clemson University.

References

1. M. YAMAGUCHI and Y. UMAKOSHI, *Prog. Mater Sci.* **34** (1990) 1.
2. M. GRUJICIC and P. DANG, *Mater. Sci. Eng.* **A224** (1997) 187.
3. A. G. EVANS and R. M. CANNON, *Acta Metall.* **34** (1986) 761.
4. G. B. OLSON, in "Innovations in Ultra-High Strength Steel Technology," edited by G. B. Olson, M. Azrin and E. S. Wright, Materials Research Conference Proceedings (Sagamore Army, 1987) p 3.
5. M. GRUJICIC and N. SANKARAN, *Int. J. Solid Struct.* **34** (1997) 4421.
6. *Idem, Int. J. Fracture* **83** (1997) 337.
7. M. GRUJICIC and Y. ZHANG, *Mater. Sci. Eng.* submitted.
8. Abaqus Theory Manual, Version 5.7, Hibbit, Karlson and Sorensen, Inc., Providence, RI, 1997.
9. A. NEEDLMAN, *J. Appl. Mech.* **54** (1987) 525.
10. D. PIERCE, R. J. ASARO and A. NEEDLMAN, *Acta Metall.* **30** (1982) 1087.
11. *Idem, ibid.* **31** (1983) 1951.
12. B. J. LEE, D. M. PARKS and S. AHZI, *J. Mech. Phys. Solids* **41** (1993) 1651.
13. R. J. ASARO and J. R. RICE, *ibid.* **25** (1977) 309.
14. B. K. KAD, M. DAO and R. J. ASARO, *Phil. Mag. A* **71** (1995) 567.
15. W. G. BURGERS, *Physica* **1** (1934) 561.
16. S. SOCRATE, PhD thesis, Massachusetts Institute of Technology (1995).
17. M. S. DAW and M. I. BASKES, *Phys. Rev. B* **29** (1984) 6443.
18. M. GRUJICIC and P. DANG, *Mater. Sci. Eng.* **A205** (1996) 139.
19. P. DANG and M. GRUJICIC, *J. Mater. Sci.* **32** (1997) 4875.
20. R. FLETCHER and C. M. REEVES, *Comput. J.* **7** (1964) 149.
21. "Pearson's Handbook of Crystallographic Data for Intermetallic Phases," Vol. 2, edited by P. Villars and L. D. Calvert (American Society for Metals, Metals Park, OH, 1985).
22. M. GRUJICIC and C. P. NARAYAN, *Mater. Sci. Eng.* **A151** (1992) 217.
23. IMSL Mathematical and Statical Libraries (IMSL, Inc., Houston, TX, 1987) pp. 780–3.
24. Y. ZHANG, Ph.D. Thesis in Progress, Clemson University, December 1998.

Received 21 July
and accepted 28 August 1998